ingegneria sismica
International Journal of Earthquake Engineering
Anno XLIII - Num. 2 - 2026

Sensor-enabled bridge health monitoring data modeling and real-time risk assessment technology research

Yunfeng Xu[1,*], *Chengfeng Tang*[2] *and Jinhua Chen*[3]

[1] School of Civil Engineering, Chongqing Jiaotong University, Chongqing, 400074, China
[2] School of Architecture and Engineering, Xinjiang University, Urumqi, Xinjiang, 830017, China
[3] School of Materials Science and Engineering, Chongqing University of Technology, Chongqing, 400074, China

SUMMARY: *The timely detection and elimination of bridge health risks are related to urban transportation and people's travel safety. In this paper, Bragg grating (BG) fiber optic sensors are selected to scan the light source and modulate the reflected signal of the bridge structure to obtain the bridge health monitoring signal source. The bridge model is constructed based on the Hilbert-Huang transform (HHT) method to identify the parameters such as the intrinsic frequency and damping ratio of the bridge structure under different degrees of freedom systems. The Wolf Pack Algorithm (WPA) is introduced to accelerate the solving speed of the optimal solution of the hierarchical weights of the BP neural network, which improves the instantaneous efficiency of the bridge health risk monitoring. The BG fiber optic sensors have better performance than the same type of sensors in the three categories of anti-electromagnetic interference, anti-drift, and anti-reciprocal anthropomorphic static force, and are able to collect the accurate bridge health data and improve the accuracy of the bridge model construction. Using the wolf pack algorithm to optimize the BP neural network, the predicted probability of risk assessment for 50 bridge parts is 0.091~0.989, which is very close to the actual 0.043~0.979.*

KEYWORDS: *BG fiber optic sensor; HHT; wolf pack algorithm; bp neural network; bridge health risk*

1 Introduction

Bridges are the key to transportation, connecting functional areas and promoting economic and social stability. They not only ensure smooth traffic flow, but also serve as city symbols, reflecting the city's image and level of development. However, long-term loading, environmental changes and aging may lead to bridge performance degradation, which may bring about safety hazards, or even cause collapse accidents or catastrophes, which may affect the life, work, health and even the safety of life and property of the local residents, and need to be monitored and managed in a timely manner in order to prevent safety hazards [1-5]. With the acceleration of urbanization and the growth of transportation demand, the number of bridges is expanding in scale, and the design complexity and environmental risks are increasing, so it is crucial to promote the research on bridge health monitoring and risk assessment in order to guarantee the efficient operation of the transportation system, to prevent public safety risks, and

*13527516308@163.com
https://doi.org/10.65102/is2026657
Published: 30 April, 2026

to ensure the long-term healthy operation of bridges [6-9]. However, the traditional monitoring methods based on manual inspection and regular maintenance have high cost, serious lag, and poor monitoring of sudden damage; and the bridge health condition data under manual inspection are seriously discrete, which is not conducive to presenting the damage evolution process [10-13]. With the continuous development of sensor technology, different types of sensors are arranged in key parts of bridges to comprehensively capture the status information of bridge structures [14]. These sensors upload data in real time through wired or wireless communication to ensure the integrity and timeliness of data transmission, laying a solid foundation for bridge health monitoring and real-time risk assessment.

Sensors have experienced a shift from resistance strain gauge phase fiber optic sensors to smart sensors with more applications today. Literature [15] reported a portable fiber optic sensor system for structural health monitoring of steel girder highway bridges, the deployment of adhesive sensors is easy to lose adhesion, which is not conducive to long-term monitoring, so the system suggests the use of conventional sensors to determine the baseline response of the bridge, and then the introduction of fiber optic sensors for the short-term health monitoring of the bridge. Literature [16] describes fiber optic sensors in structural health monitoring of bridges that are capable of measuring parameters such as bridge deformation, temperature, and strain to provide real-time continuous data, but there are challenges in installation, calibration, and data interpretation. Literature [17] provided long-term monitoring of large fatigue cracks in bridges via wireless large area strain sensors and created an algorithm for processing and converting data collected by the sensors under traffic loading that was able to track potential fatigue crack expansion. Literature [18] claims that nanosensors have been used to measure and monitor physical properties such as volume, concentration, movement, velocity, gravity, and environmental parameters of bridge structures at the molecular level to analyze and assess bridge structural health and integrity. However, the complexity of bridge structures and the variety of operating environments make it difficult for a single sensor to acquire comprehensive data and difficult to integrate and analyze heterogeneous data from multiple sources, leading to challenges in monitoring.

Gradually, researchers have fused multiple sensor data to improve the accuracy of bridge health monitoring. Literature [19] used multiple accelerometer sensors to obtain the power spectral density and harmonic occurrence frequency of bridge vibration signals under traffic loads in real time, so as to assess the decline of bridge stiffness and realize the monitoring of bridge structural health. Literature [20] designed an integrated sensor based on GNSS and accelerometers to improve the accuracy of deformation and vibration measurements of bridges in bridge monitoring, but the low-cost accelerometers are insufficient to detect the frequency of weak motion of bridges. Literature [21] provides a multi-source heterogeneous data integration scheme for large-scale bridge health monitoring system, which is able to process and fuse multi-sensor data, and has good reliability and stability in the monitoring practice of Jiujiang Yangtze River Highway Bridge. Literature [22] proposed a vibrating cantilever beam wireless sensor to realize Internet of Things (IoT)-based health monitoring of small bridges by signaling the signals collected during bridge vibration and transmitting the data wirelessly. Literature [23] constructed an IoT-based bridge health monitoring system using sensor data for real-time monitoring of bridge changes and introduced the K-nearest neighbor algorithm based on the sensor monitoring data for bridge maintenance and management decisions.

In bridge risk assessment, the bridge data monitored by sensors and other risk influencing factors are mainly used for comprehensive assessment. Literature [24] constructed a machine learning-based prediction model for assessing bridge load carrying capacity using real-time sensor data, and this assessment framework helps in real-time continuous health monitoring of

bridge structures and risk assessment of load carrying deficiencies. Literature [25] set adaptive water level thresholds based on monitoring data with a structural sensor-based scour monitoring system for assessing bridge scour risk and assisting bridge management in controlling traffic closure. Literature [26] integrated wireless sensor networks, fiber optic sensors, and digital image technology to assess the safety of bridges under long-term operating conditions and proposed a safety management strategy to improve the safety of bridges under long-term service risk. Literature [27] used laser distance sensors for bridge displacement monitoring, established a digital twin structural model to simulate the risk of different reinforced concrete bridges so as to quantitatively assess the potential risk of bridges, and proposed a bridge risk management framework. Literature [28] combined bridge structural testing experiments, finite element methods, multi-sensor data fusion, back-propagation neural networks, and principal component analysis for assessing the progressive collapse risk of steel pipe fastener scaffold bridges. Literature [29] used multi-source sensor data fusion technology and BeiDou high-precision positioning technology to create a real-time monitoring and early warning system for bridge collapse risk, which reduces the risk of bridge collapse through real-time risk perception, dynamic risk assessment, and rapid risk warning. Literature [30] relied on multi-source data fusion based on sensing and monitoring technologies, and constructed a system digital twin framework using Bayesian network modeling for full life cycle risk assessment of bridge networks under different scenarios. However, effective processing of health monitoring data and real-time risk assessment remain the current challenges in bridge monitoring and management.

In this paper, Bragg grating (BG) fiber optic sensors are used to collect and modulate the optical property parameters of different bridge locations, and through the wavelength difference of the reflected back, to demodulate the characteristics of the optical signals at the measured location, which can sensitively reflect the health condition of the bridge. Incorporating the Hilbert-Huang Transform (HHT) method and the stochastic reduction technique, the structural modal parameters of the health detection signals from different parts of the bridge are processed and identified to realize the digital modeling of the bridge health. The wolf pack algorithm with global search and optimization ability is selected to optimize the BP neural network, and the optimization is sought through the weights of each layer of the network, so as to improve the performance of the bridge model risk detection of the BP neural network, and to discover the risks of the bridge in time.

2 Sensor data-based bridge modeling and risk monitoring technology implementation

2.1 Components and principles of fiber optic sensors

2.1.1 Principles of composition

Fiber optic sensors are mainly composed of light source, optical fiber and detector. The light from the light source coupled into the optical fiber, through the fiber into the modulation zone, in the modulation zone, the external parameters to be measured in the modulation zone into the light signal, so that its optical properties such as light intensity, phase, frequency, polarization, wavelength, etc. changes to become a modulated signal light, and then through the optical fiber into the optical detector to obtain the measured parameters. Fiber optic sensors in the optical fiber is usually composed of core, cladding, resin coating and plastic sheath. The core and cladding have different refractive indices, and the resin coating protects the fiber. Optical fiber is divided into glass fiber and plastic fiber according to the composition of the material;

according to the fiber core and cladding refractive index distribution can be divided into step refractive index optical fiber and gradient refractive index optical fiber two. Optical fiber can constrain and guide light waves to propagate forward along the axis direction near its interior or surface, with the dual functions of sensing and transmission, which is a very important smart material. Figure 1 shows the transmission principle of step refractive index optical fiber. Optical fibers work on the principle of total reflection of light.

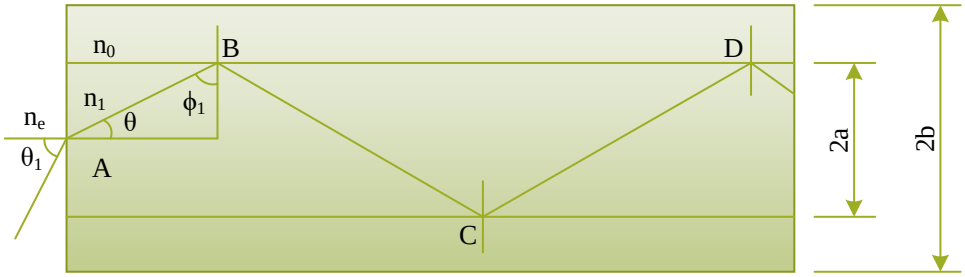

Figure 1: Transmission Principle of Step-Index Fiber

Let the refractive index of air be n_0, the refractive index of the fiber core be n_1, and the refractive index of the cladding be n_2. When incident light of wavelength n is incident on the end face of a cylindrical fiber at θ_0, it is known by the law of refraction:

$$n_0 \sin\theta_0 = n_1 \sin\theta_1 \cos\varphi_1 \tag{1}$$

When $n_1 > n_2$, the critical angle φ_c at which total reflection occurs when light is directed from the core to the cladding is determined by the following equation:

$$\sin\varphi_c = n_2 / n_1 \tag{2}$$

Therefore, light is required when total reflection occurs at the core and cladding interface:

$$\sin\varphi_1 > \sin\varphi_c = \frac{n_2}{n_1} Or \cos\varphi_1 < \sqrt{1-\left(\frac{n_2}{n_1}\right)^2} \tag{3}$$

Substituting equation (3) into equation (1) gives:

$$\sin\theta_0 < \frac{1}{n_0}\sqrt{n_1^2 - n_2^2} \tag{4}$$

Since the refractive index n_0 of air is approximated to be 1.0, there are

$$\theta_0 < \arcsin\sqrt{n_1^2 - n_2^2} = \theta_m \tag{5}$$

The above equation determines the range of angles of incidence of light at the end face that can produce total reflection to be $2\theta_m$, and when the angle of incidence θ_0 is within this range, the light produces total reflection at the interface and is repeatedly reflected again and again,

one by one, inside the fiber, at the same angle, until it propagates to the other end face of the fiber. If the work requires a slight bend in the fiber, the light can still proceed as long as the law of total reflection is still satisfied. If the angle of incidence θ_0 is outside of the above range, the light entering the fiber is refracted at the interface and penetrates into the cladding.

There are many types of fiber optic sensors, according to the role of fiber optic sensors in the fiber optic sensor can be divided into two types of sensing and light transmission type. Sensing fiber optic sensors, also known as functional fiber optic sensors, the main use of single-mode optical fiber, optical fiber not only plays a role in transmitting light, at the same time is a sensitive element, which uses the transmission characteristics of the optical fiber itself is measured by the role of physical quantities and changes in the characteristics of the optical waveguide attributes (light intensity, phase, polarization state, wavelength, etc.) is modulated. Therefore, this type of fiber optic sensor is divided into light intensity modulation type, phase modulation type, polarization state modulation type and wavelength modulation type and so on. For sensing type fiber optic sensors, high sensitivity can be obtained by lengthening the length of the optical fiber because the optical fiber itself is the sensitive element. Light transmitting fiber optic sensors, also known as non-functional fiber optic sensors, measure the optical signal modulated by the object to be measured by inputting it into the optical fiber and then measuring it by processing the optical signal at the output end. In this type of sensor, the optical fiber is only used as a light-transmitting element, and a sensitive element that can modulate the light transmitted by the optical fiber must be attached in order to form a sensing element.

2.1.2 Bragg Grating (BG) Fiber Optic Sensors

1) Bragg grating sensor features

Bragg grating sensor belongs to wavelength modulation type nonlinear action sensor. Bragg grating fiber will be quasi-monochromatic ray source from a particular angle of incidence in the crystal, all the reflected light concentrated in a particular direction. The wavelength of the incident beam is modulated by the to-be-measured modulation, and the wavelength change of the reflected light is measured for detection. Since the wavelength is an absolute parameter that is not affected by the overall light intensity level, losses at the connecting fiber and coupler, or the energy of the light source, it is more stable than other light modulation methods. Bragg grating fiber optic sensors are quasi-distributed sensors formed by periodically changing the refractive index of the core along the fiber axial direction within a section of the fiber. In a fiber at different locations can be written in many different grating pitch Bragg grating, easy to achieve code division, wavelength division and other multiplexing techniques, can connect the number of Bragg grating by the light source bandwidth limitations.

Bragg grating is a part of the communication fiber using germanium-doped fiber nonlinear absorption effect of the UV holographic exposure method and made a kind of refractive index of the core known as Bragg grating (BG) periodic changes in the grating. All normal light passes through the BG unaffected, and only light of a specific wavelength (λ_b) is reflected at the BG and then returned to its original direction. When an external force is applied to the Bragg grating and the spacing of the grating changes, the wavelength of the reflected light will change accordingly.The Bragg wavelength λ_b is affected by both the Bragg grating period and the effective refractive index of the fiber core perturbation, and thus strain and temperature perturbation can be measured by monitoring the change of the Bragg wavelength.

When strain ε occurs in the fiber, $\Lambda_1 = \Lambda(1+\varepsilon)$, which can be derived from the theory of photoelasticity

$$\frac{1}{\lambda_b}\frac{\Delta\lambda_b}{\Delta\varepsilon} = 0.81\times10^{-5} / \mu\varepsilon \tag{6}$$

For specific wavelengths

$$S_b = \frac{\Delta\lambda_b}{\Delta\varepsilon} = 0.81\times10^{-5}\lambda_b(mm/\mu\varepsilon) \tag{7}$$

is the Bragg grating strain sensitivity, i.e., the Bragg grating gives $S_b(mm)$ wavelength shift for each microstrain. When the fiber undergoes a temperature change ΔT, the temperature not only causes a change in the refractive index of the grating, but also changes the Bragg grating pitch at the same time, from which it can be derived that

$$\frac{\Delta\lambda_b}{\lambda_b} = (\alpha+\xi)\cdot\Delta T \tag{8}$$

where α and ξ are the thermal expansion coefficient of the fiber and the thermo-optic coefficient of the germanium-doped fiber, respectively. For a specific wavelength

$$S_T = \frac{\Delta\lambda_b}{\Delta T} = (\alpha+\xi)\cdot\lambda_b(mm/K) \tag{9}$$

is the Bragg grating temperature sensitivity, i.e., the Bragg grating gives $S_T(mm)$ wavelength shift for each unit temperature change.

2) Fiber Grating Sensing Network Solutions

In order to measure individual temperature changes or strain values, one of the solutions is to build a network of multi-channel sensing systems to realize multi-point measurements as well as to find out the unique corresponding values of parameter changes. Figure 2 shows the working principle of the multichannel sensing network. The sensing network is characterized by fast response speed, high sensitivity and high measurement accuracy. Light from the light source, after beam splitting, one way light as a reference light into the signal analyzer, the other way light through the fiber grating sensor and then back to the signal analyzer, through the comparison between the two optical signals and processing can be demodulated out of the measured signal.

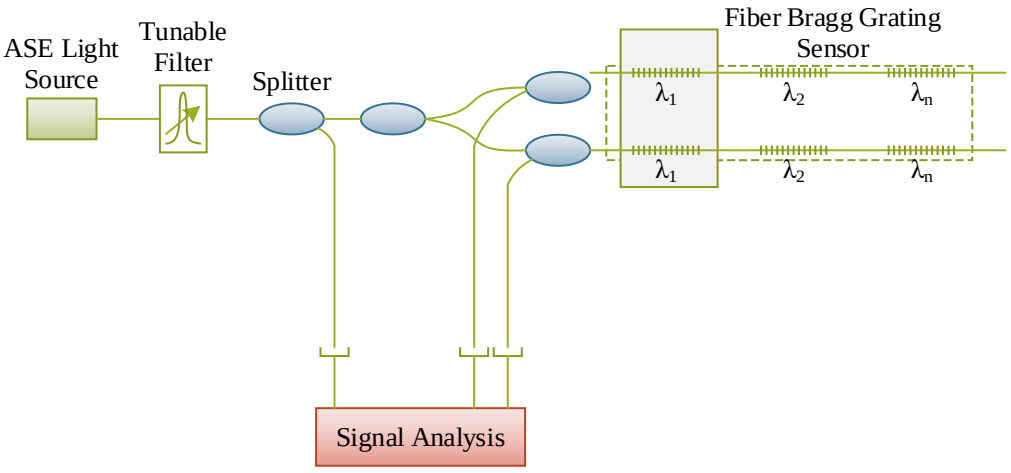

Figure 2: Multi-channel Sensor Network

For the fiber grating sensor, has solved the fiber grating irradiation technology, now the research focuses on the signal demodulation and analysis of the sensing network, because the fiber grating sensor changes the amount of wavelength, so we should use the corresponding wavelength detector meter or optical spectrum analyzer to detect, or the wavelength of the sensing network for precise control. For multi-channel sensing network, to realize the large-scale sensing network data processing, we must use some corresponding complex equipment.

2.2 Identification of modal parameters of bridge structure based on HHT

2.2.1 Single-degree-of-freedom systems

As an example, the displacement response of a single-degree-of-freedom linear system subjected to impact loading is:

$$X(t) = A_0 e^{-\xi\omega t}\cos(\omega_d t + \varphi_0) \tag{10}$$

where ω is the circular frequency, ω_d is the damping frequency, and ξ is the damping ratio. The analytic signal $Z(t)$ corresponding to $X(t)$ is:

$$Z(t) = X(t) + iY(t) = A(t)e^{-i\theta(t)} \tag{11}$$

where $Y(t)$ is the HT transform of $X(t)$, and for general engineering structures, the amplitude $a(t)$ and phase angle $\theta(t)$ can be further expressed as:

$$A(t) = A_0 e^{-\xi\omega t}, \quad \theta(t) = \omega_d t + \varphi_0 \tag{12}$$

Introducing logarithmic and differential operators to the above equation, respectively, yields:

$$\ln A(t) = -\xi\omega t + \ln A_0 \tag{13}$$

$$\omega = \frac{d\theta(t)}{dt} = \omega_d \tag{14}$$

2.2.2 Multi-degree-of-freedom systems

The equations of structural dynamics for n degrees of freedom under impact loading can be expressed as:

$$[M]\{\ddot{X}(t)\} + [C]\{\dot{X}(t)\} + [K]\{X(t)\} = \{F(t)\} \tag{15}$$

where $\{X(t)\} = [x_1, x_2, \cdots, x_n]^T$ is the n-dimensional displacement vector, $\{F(t)\}$ is the n-dimensional force vector, $[M]$, $[C]$, and $[K]$ are the $n \times n$-dimensional mass, damping, and stiffness matrices, respectively. Assuming the existence of normalized modes of the structure, the displacement and acceleration responses can be decomposed into n real modes:

$$\{X(t)\} = [\Phi]\{q\} \tag{16}$$

where $[\Phi]$ is the modal matrix and $\{q\}$ is the modal coordinate. Substituting Eq. (16) into Eq. (15) and using the orthogonality property of the vibration mode is known:

$$\ddot{q}_j + 2\xi_j \omega_j \dot{q}_j + \omega_j^2 q_j = \Phi_j^T F(t)/m_j \tag{17}$$

where ω_j is the j th order modal frequency, ξ_j is the j th order modal damping ratio, and m_j is the j th order modal mass.

If an impact load acts on the k th degree of freedom of the structure, that is, $f_k(t) = F_0\delta(t)$ and $f_j(t) = 0(j \neq k)$, the j th acceleration response, expressed in modal coordinates, is:

$$\ddot{q}_j(t) = \frac{F_0 \phi_{kj} \omega_j}{m_j \sqrt{1-\xi_j^2}} e^{-\xi_j \omega_j t} \cos\left(\omega_{dj} t + \varphi_j + \frac{\pi}{2}\right) \tag{18}$$

where ϕ_{kj} is the k th element of the j th modal vector Φ_j, $\omega_{dj} = \omega_j\sqrt{1-\xi_j^2}$ is the j th damping frequency, and $\varphi_j = \tan^{-1}\left[2\xi_j\sqrt{1-\xi_j^2}\Big/\left(1-2\xi_j^2\right)\right]$ is the j th modal phase difference angle. Then, the $p(p=1,2...n)$ order acceleration response is:

$$\ddot{x}_p(t) = \sum_{j=1}^{n} \phi_{pj} \ddot{q}_j(t) = \sum_{j=1}^{n} \ddot{x}_{pj}(t) \tag{19}$$

Eq.

$$\ddot{x}_{pj}(t) = \phi_{pj}\ddot{q}_j(t) = B_{pj,k} e^{-\xi_j \omega_j t} \cos\left(\omega_{dj} t + \varphi_j + \frac{\pi}{2} + \varphi_{pj,k}\right) \tag{20}$$

$$B_{pj,k} = \frac{F_0 \left|\phi_{pj}\right|\left|\phi_{kj}\right| \omega_j}{m_j\sqrt{1-\xi_j^2}} \tag{21}$$

where $\varphi_{pj,k}$ is the phase difference between the p and k elements of the j th order vibrational mode of the structure. Since standard modes exist and all vibrational modes are real, the phase angle $\varphi_{pj,k}$ is equal to $\pm 2m\pi$ or $\pm 2(m+1)\pi$, with m being a positive integer, i.e:

$$\begin{aligned} &\varphi_{pj}/\varphi_{kj} > 0, \quad Which\ \varphi_{pj,k} = \pm 2m\pi \\ &\varphi_{pj}/\varphi_{kj} < 0, \quad Which\ \varphi_{pj,k} = \pm 2(m+1)\pi \end{aligned} \tag{22}$$

Any system identification method should be able to handle noise contaminated data due to the high level of noise interference that actually exists. The measured acceleration response vector $\ddot{Z}(t) = [\ddot{z}_1(t), \ddot{z}_2(t), ..., \ddot{z}_n(t)]^T$ can be expressed as:

$$\ddot{Z}(t) = \ddot{X}(t) + V(t) \tag{23}$$

where $V(t)=[v_1(t),v_2(t),...,v_n(t)]^T$ is the white noise vector. Under impact loading the structure at $p(p=1,2.....n)$ order acceleration response can be expressed as:

$$\ddot{z}_p(t)=\ddot{x}_p(t)+v_p(t)=\sum_{j=1}^{n}\ddot{x}_{pj}(t)+v_p(t) \tag{24}$$

where $v_p(t)$ can be treated as a zero-mean Gaussian white noise with finite bandwidth.

The acceleration response $\ddot{z}_p(t)$ can be decomposed into the sum of m intrinsic mode functions (IMFs) c_{pj} and the residual term r_p using EMD decomposition:

$$\ddot{z}_p(t)=\sum_{j=1}^{m}c_{pj}(t)+r_p(t) \tag{25}$$

Because of the presence of noise, the eigenmode function $c_{pj}(t)$ here is not the structural modal response $\ddot{x}_{pj}(t)$. If the structural modal response is $\ddot{x}_{pj}(t)\,(j=1,2,...,n)$, then the measured acceleration response can be further decomposed as:

$$\ddot{z}_p(t)=\sum_{j=1}^{n}\ddot{x}_{pj}(t)+\sum_{j=1}^{m-n}c_{pj}(t)+r_p(t) \tag{26}$$

Combining Eqs. (20)-(21), the HT transformation of $\ddot{x}_{pj}(t)$ is:

$$\begin{aligned}Y_{pj}(t)=B_{pj,k}\Bigg[&a_{LP,j}(t)\sin\left(\omega_{dj}t+\varphi_j+\frac{\pi}{2}+\varphi_{pj,k}\right)\\&+a_{HP,j}(t)\cos\left(\omega_{dj}t+\varphi_j+\frac{\pi}{2}+\varphi_{pj,k}\right)\Bigg]\end{aligned} \tag{27}$$

Eq.

$$\begin{aligned}a_{LP,j}(t)&=\frac{1}{\pi}\int_{-\infty}^{+\infty}\frac{2\xi_j\omega_j}{\xi_j^2\omega_j^2+\omega^2}\cos(\omega x)d\omega\\a_{HP,j}(t)&=\frac{1}{\pi}\int_{-\infty}^{+\infty}\frac{2\xi_j\omega_j}{\xi_j^2\omega_j^2+\omega^2}\sin(\omega x)d\omega\end{aligned} \tag{28}$$

The analytic solution for the j th order modal of the structure can be expressed as:

$$Z_{pj}(t)=\ddot{x}_{pj}(t)+iY_{pj}(t)=A_{pj}(t)e^{-i\theta_{pj}(t)} \tag{29}$$

where $A_{pj}(t)$ is the instantaneous amplitude and $\theta_{pj}(t)$ is the instantaneous phase angle, which can be expressed as:

$$A_{pj}(t)=B_{pj,k}e^{-2\xi_j\omega_j t}\left\{\cos^2\left(\omega_{dj}t+\varphi_j+\frac{\pi}{2}+\varphi_{pj,k}\right)+\left[a_{LP,j}(t)\sin\left(\omega_{dj}t+\varphi_j+\frac{\pi}{2}+\varphi_{pj,k}\right)+a_{HP,j}(t)\cos\left(\omega_{dj}t+\varphi_j+\frac{\pi}{2}+\varphi_{pj,k}\right)\right]^2\right\}^{1/2} \tag{30}$$

$$\theta_{pj}(t)=\tan^{-1}\left\{e^{\zeta_j\omega_j t}\left[a_{LP,j}(t)\tan\left(\omega_{dj}t+\varphi_j+\frac{\pi}{2}+\varphi_{pj,k}\right)+a_{HP,j}(t)\right]\right\} \tag{31}$$

Assuming that the damping ratio ξ_j is very small and the modal frequency ω_j is large, it follows from Eq. (29):

$$a_{LP,j}(t)\approx e^{-\zeta_j\omega_j t};\ a_{HP,j}(t)\approx 0 \tag{32}$$

Thus, Eq. (28) can be changed to:

$$Y_{pj}(t)=B_{pj,k}e^{-\zeta_j\omega_j t}\sin\left(\omega_{dj}t+\varphi_j+\frac{\pi}{2}+\varphi_{pj,k}\right) \tag{33}$$

Meanwhile, the instantaneous amplitude and instantaneous phase angle determined by Eq. (31) can be expressed as:

$$A_{pj}(t)=B_{pj,k}e^{-2\zeta_j\omega_j t};\ \theta_{pj}(t)=\omega_{dj}t+\varphi_j+\frac{\pi}{2}+\varphi_{pj,k} \tag{34}$$

From equation (34), we have:

$$\ln A_{pj}(t)=-\xi_j\omega_j t+\ln B_{pj,k} \tag{35}$$

$$\omega_j(t)=d\theta_{pj}(t)/dt=\omega_{dj} \tag{36}$$

2.2.3 Identification of intrinsic frequency and modal damping ratio

From Eqs. (13) and (32), the linear equation of phase angle versus time can be fitted by the least squares method, and the slope of the straight line is the damping frequency ω_d (or ω_{dj}) of the structure; similarly, from Eqs. (13) and (31), the slope of the linear equation of amplitude versus time is $-\xi\omega$ (or $-\xi_j\omega_j$); after finding ω_d (or ω_{dj}), $-\xi_j\omega_j$ (or $-\xi_j\omega_j$), the slope of the linear equation of amplitude versus time is given by $\omega_d=\omega\sqrt{1-\xi^2}$ (or $\omega_{dj}=\omega_j\sqrt{1-\xi_j^2}$) the circular frequency ω (or ω_j) and damping ratio ξ (or ξ_j) can be found.

When the structural modal damping ratio is large, the fluctuations of the amplitude $\ln A_{pj}(t)$

around the least-squares fitted straight line are very significant (actually nonlinear). In this case, since the residual term $r_p(t)$ represents the mean trend term of $\ln A_{pj}(t)$, the slope $-\xi\omega$ (or $-\xi_j\omega_j$) can be estimated from the residual term from the least squares fitted curve.

For the environmental random excitation, the modal response of the structure after EMD decomposition actually consists of two parts: the free vibration response and the forced vibration response caused by external loads. The free vibration response can be obtained by applying the stochastic reduction technique to these modes. For this free vibration response, the same steps as for the identification of the parameters of the single degree of freedom system can be used to find the frequency and damping ratio of each order of the system.

In addition, after obtaining the modal response component IMF of the structure, the instantaneous frequency or center frequency of the structure can be obtained through the time-frequency spectrum and the marginal spectrum, and even the modal frequency of the structure can be obtained through the FFT transform. If the response of all degrees of freedom of the structure can be measured, the structural vibration mode, mass matrix, damping matrix and stiffness matrix can be further identified. Figure 3 shows the process flow of HHT parameter identification.

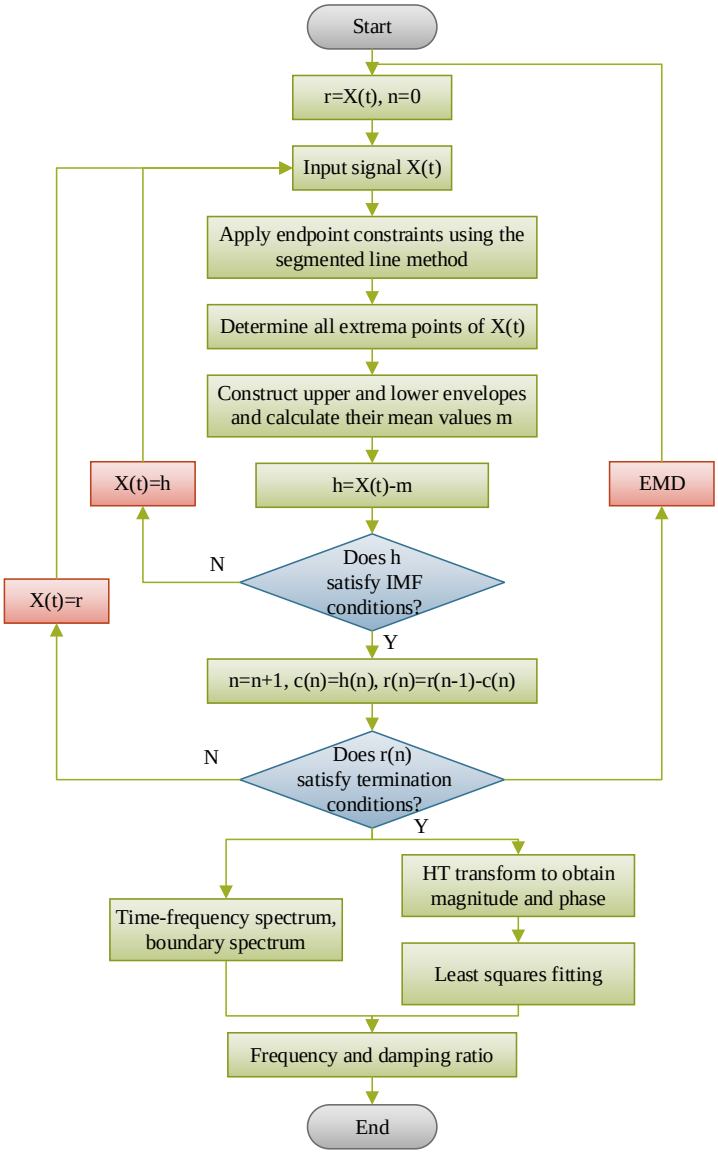

Figure 3: Flowchart of Parameter Identification Process for HHT Method

2.3 Optimization of bridge real-time risk assessment algorithm and construction of assessment index system

2.3.1 Wolfpack Algorithm Principles and Steps

The wolf pack algorithm (WPA) is used to optimize the BP neural network to improve the real-time risk assessment ability of the BP neural network on the bridge model, and to determine whether the risk indicator data of the bridge is within the range of change.

The wolf pack algorithm divides the wolf pack into three main categories: head wolf, scout wolf and fierce wolf. The head wolf is the command center of the wolf pack and is responsible for making overall decisions based on the prey information perceived by the wolf pack. The probing wolf is responsible for detecting the prey information within the range of prey activities, and always pursues the prey in the direction of the greatest concentration of prey odor. The scout wolf reports to the head wolf when it finds the prey, and the head wolf processes the information sent by the scout wolf and summons the fierce wolves to attack the prey by howling.

In the search space, n wolves with good objective function values are selected as campaign wolves, and the wolf at the optimal search position is selected as the first wolf through search. This process is the "winner-takes-all" rule for generating the leader wolf. The other m wolves are selected as scout wolves, and move towards the leader wolf. When the concentration of prey odors detected by the probing wolf is greater than the concentration of prey odors detected by the head wolf, the head wolf is replaced. This forward process is referred to as the wandering behavior of the probing wolf. When the probing wolf detects a prey trail and the head wolf receives a report from the probing wolf, the head wolf summons the fierce wolf to approach the prey by howling. This process is known as the calling behavior of the head wolf. During the process of approaching the prey, the replacement of the mastodon that sniffed out the prey with a greater odor concentration than the head wolf became the new head wolf and re-initiated the howling. At a certain distance from the prey, the wolves gathered around the head wolf and started searching for the prey. This behavior is referred to as the mobbing behavior of the wolves. After the prey is captured, it is distributed from the strongest to the weakest, and a few weak wolves die of starvation due to lack of food, so the pack needs to be replenished. This process is known as the "survival of the strongest" mechanism of pack renewal.

The implementation steps of the wolf pack algorithm are divided into the following six main points:

1) Wolf pack initialization. The main purpose of wolf pack initialization is to make the wolves evenly distributed in the target space. Set the search space dimension D of the algorithm, the number of individual wolves N, the wolf scouting proportion factor α, the maximum number of wandering times $T_{\max}$, the step length factor S, the wolf update proportion factor β, the distance determination factor w and the maximum number of iterations $K_{\max}$ of the algorithm. Then the initial position of each artificial wolf in the space is:

$$\begin{aligned} &X_i = \left(X_{i1}, \cdots, X_{id}, \cdots, X_{iD}\right), i = 1, 2, \cdots, N \\ &X_{id} = X_{\min} + rand\left(X_{\max} - X_{\min}\right) \end{aligned} \tag{37}$$

where $rand$ is a random number uniformly distributed on the interval $[0,1]$, and $X_{\max}$ and $X_{\min}$ are the maximum and minimum search ranges of the search space, respectively.

2) Campaigning for the head wolf. Calculate the objective function value of each wolf through the objective function, and select the one with the best function value as the head wolf.

3) Wandering behavior. According to the objective function value, the m wolf with the best objective function value except the head wolf is selected as the scouting wolf. The m is a random integer in the interval $[n/(\alpha+1), n/\alpha]$, and α is the scaling factor of the probing wolf. The probing wolf searches in H directions around itself according to the following equation. During the search process, the probing wolf that replaces the one whose sniffed prey odor concentration O_i is greater than the head wolf's sniffed odor concentration O_{lead} becomes the head wolf, and when the number of tours T reaches the maximum number of tours $T_{\max}$, the search is terminated, and the wolf with the optimal position is taken as the head wolf. Where the position $X_{i,d,h}$ of the i th probing wolf in the d th dimension after searching in the h direction is:

$$X_{i,d,h} = X_{id} + \sin(2\pi \times h / H) step_{a,d}, h = 1, 2, \ldots, H \tag{38}$$

where $step_{a,d}$ represents the search step of the probing wolf on the d th dimension.

4) Running behavior. The head wolf calls the fierce wolf according to its optimal position, and the fierce wolf runs towards the head wolf. Where the position of the i th fierce wolf at the m th iteration is:

$$X_{i,d,m+1} = X_{i,d,m} + step_{b,d}\left(G_{d,m} - X_{i,d,m}\right), d = 1, 2, \ldots, D \tag{39}$$

where $G_{d,m}$ is the location of the head wolf in d -dimensional space, and $step_{b,d}$ is the search step of the Mastodon in the d th dimension.

During the run of the Mastodon, the Mastodon that replaces the one that sniffs out the prey odor concentration O_i greater than the head wolf's sniffing out odor concentration O_{lead} becomes the head wolf, and is re-summoned. If the head wolf is not replaced, the manticore continues to approach the head wolf until the manticore's distance $d_{i,d}$ from the prey is less than or equal to d_{near}. where d_{near} represents the minimum search distance within the search range $[\min_d, \max_d]$ in the d dimension:

$$d_{near} = \frac{1}{D \times w} \cdot \sum_{d=1}^{D} \left| \max_d - \min_d \right| \tag{40}$$

5) Siege behavior. After the summoning behavior, the fierce wolves and scout wolves gather around the head wolf and conduct a close search to capture the prey. At this time, set the prey location that is the location of the head wolf, then for the m th generation of wolves, the siege behavior can be expressed as:

$$X_{i,d,m+1} = X_{i,d,m} + \lambda \times step_{c,d} \times \left| g_{d,m} - X_{i,d,m} \right| \tag{41}$$

where λ is a random number uniformly distributed on the interval $[-1.0,1.0]$, $step_{c,d}$ is the step length when the wolves perform the siege behavior, and $g_{d,m}$ is the position of the prey in the d-dimensional space.

After the siege behavior, if the concentration of the prey odor smelled by the artificial wolf becomes thicker, the position of the artificial wolf will be updated, and vice versa, no need to update. Finally, the artificial wolf with the largest adaptation degree, i.e., the largest odor concentration, is selected as the head wolf.

6) Wolf Pack update. After capturing the prey, food is distributed according to the principle of "from strong to weak", resulting in the elimination of the underperforming R weak wolves due to the lack of food allocation. At the same time, an equal number of artificial wolves are generated to supplement the pack and maintain the diversity of the pack structure. R is a random integer within the range of $[n/(2\times\beta), n/\beta]$, where β is the update scale factor.

The whole algorithm has a functional relationship between the wandering step length $step_{a,d}$ of the probing wolf, the running step length $step_{b,d}$ of the fierce wolf, and the siege step length $step_{c,d}$, as follows:

$$step_{a,d} = step_{b,d}/2 = 2step_{c,d} = \left|X_{d,\max} - X_{d,\min}\right|/S \tag{42}$$

where S is the step factor, $X_{d,\max}$ and $X_{d,\min}$ are the maximum and minimum search range values of the search space on the d-dimensional space.

After the algorithm processing, the algorithm accuracy and the number of iterations are judged, if the requirements are met or the maximum number of iterations is reached, then the algorithm ends and outputs the optimal solution, i.e., the location of the head wolf, otherwise the operation from step (2) to step (5) continues to be executed. Figure 4 shows the flow of the wolf pack algorithm.

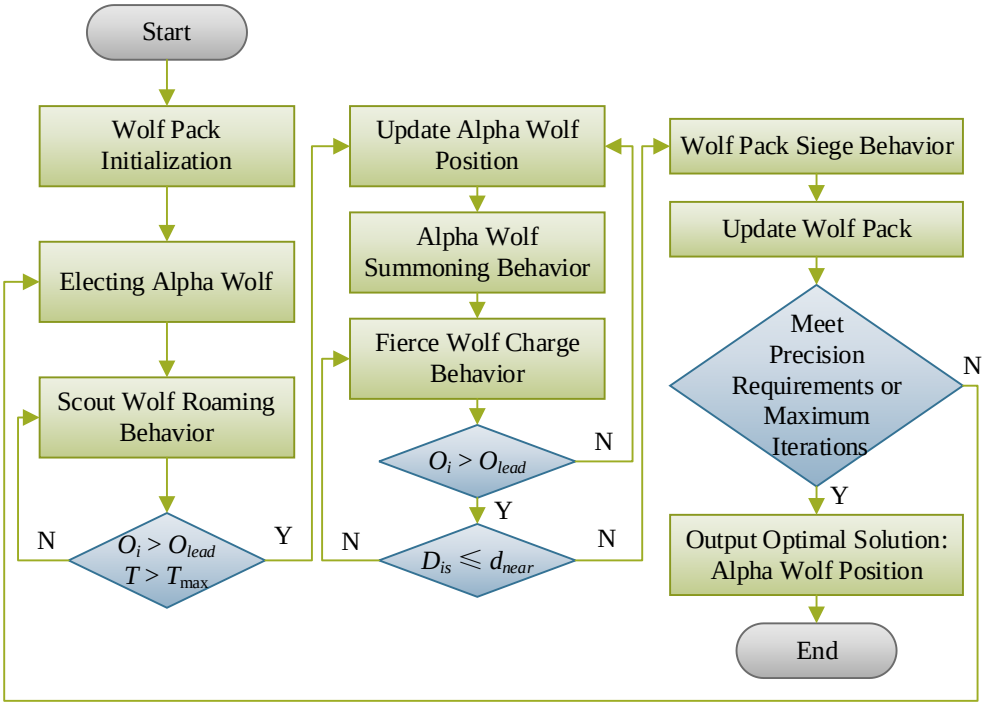

Figure 4: Flowchart of the Wolf Pack Algorithm

2.3.2 BP Neural Network Optimized by Wolf Pack Algorithm

One of the reasons why the BP neural network algorithm converges slowly and the difference between the predicted results and the actual results in real-time detection and assessment of bridge health risk is due to the random initialization of the weights and thresholds of each layer in the neural network. The wolf pack algorithm has a good global search capability in the target range space, and can iteratively find the optimal solution in the spatial range. Therefore, this paper uses the wolf pack algorithm to optimize the BP neural network, determine the weights and thresholds in each layer of the neural network, and achieve the purpose of improving the convergence speed and prediction accuracy of the BP neural network.

Figure 5 shows the WPA-BP algorithm flow. The core of the wolf pack algorithm to optimize the BP neural network is the iterative optimization search through the wolf pack algorithm, and the optimization search results are used as the initial weights and thresholds of the BP neural network, and then the BP neural network is used to train and learn the data, and ultimately to achieve the classification and prediction of the data.

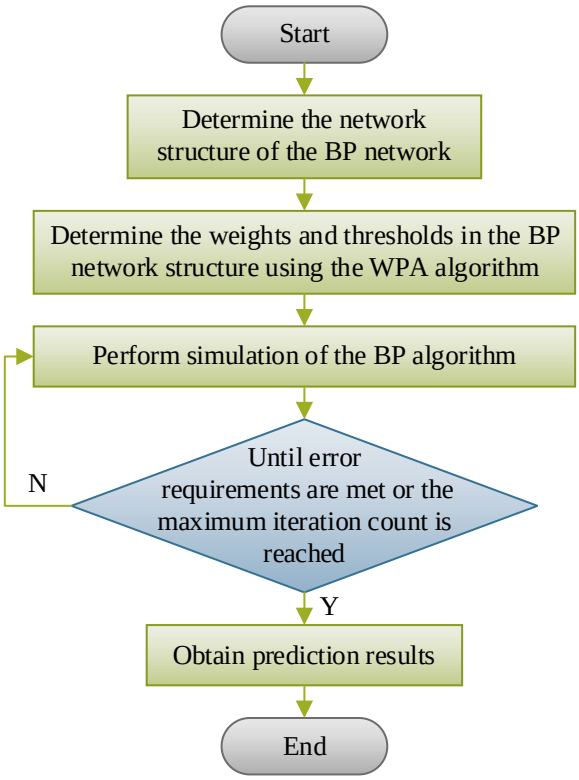

Figure 5: Workflow of WPA-BP Algorithm

2.3.3 Bridge Risk Indicator System Construction and Range of Indicator Changes

According to the structural characteristics of the bridge and related parameters, as well as the collected bridge health monitoring data, the bridge risk indicator system in Table 1 is constructed and the range of indicator changes is clarified. The bridge risk indicators include: strain, temperature, impact load, displacement amplitude, displacement phase angle, material stiffness, NIR, instantaneous frequency, center frequency, relative humidity, concrete carbonation, corrosion of reinforcement, a total of 12 items, and the scope of change of each indicator includes five tiers, and the further the tier, the higher the likelihood of the bridge to appear health risks.

Table 1: Risk indicator system and indicator variation range

Risk indicator	Range of variation				
Strain (με)	-500.0	-250.0	0.0	250.0	500.0
Temperature (℃)	32.5	35.0	37.5	40.0	42.5
Impact load (%)	5.0	6.0	7.0	8.0	9.0
Displacement amplitude (mm)	30.0	60.0	90.0	120.0	150.0
Displacement phase angle (°)	3.0	3.5	4.0	4.5	5.0
Material stiffness (%)	2.0	3.0	4.0	5.0	6.0
Nirabhi	0.1	0.2	0.3	0.4	0.5
Instantaneous frequency (%)	15.0	20.0	25.0	30.0	35.0
Center frequency (%)	10.0	15.0	20.0	25.0	30.0
Relative humidity (%)	25.0	35.0	45.0	55.0	65.0
Concrete carbonation (%)	3.0	4.5	6.0	7.5	9.0
Rebar corrosion (%)	5.0	7.5	10.0	12.5	15.0

3 Sensor-supported bridge modeling and risk assessment technology applications

3.1 BG fiber optic sensor basic performance test

3.1.1 Comparison of anti-electromagnetic interference performance

In this section, the basic performance of BG fiber optic sensors is verified at different levels, firstly, the basic performance tests of BG fiber optic sensors against electromagnetic interference and zero drift are carried out, and then the feasibility and reliability of the BG fiber optic sensors in the actual structure are verified on the coagulation test model. At the same time, RDA inclination sensor and FBG strain sensor are selected as comparison sensors to compare the differences in the basic performance of the three types of sensors.

The switching walkie-talkie was subjected to electromagnetic interference for a duration of 900s in a range of 2.5m around the sensor, and Fig. 6 shows the comparison of the strain situation of the 3 types of sensors. From the strain situation of the 3 types of sensors, the RDA inclination sensor is the most affected by electromagnetic interference, and the fluctuation of -1373.586~1197.115 με occurs throughout the experimental process, which is far more than the variation range of the strain risk indicator of -500~500με. The fluctuation range of the FBG strain sensor is between -466.327~543.294 με, which is better than that of the RDA inclination sensor in terms of EMI resistance, but also slightly exceeds the variation range of the strain risk indicator.The BG fiber-optic sensor has the best EMI resistance among the three types of sensors, with strain fluctuations of about -108.659~147.991 με.

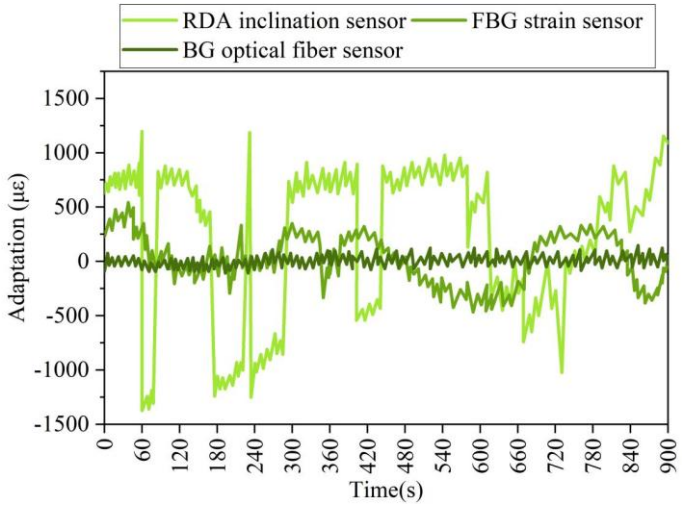

Figure 6: Comparison of strain conditions of the three types of sensors

3.1.2 Comparison of anti-drift performance

At a constant ambient temperature, the equal-strength beam was placed in an unstressed state, and the changes of the three types of strain sensors affixed to it were observed within 3 hours. Figure 7 shows the comparison of the anti-zero drift performance of the three types of sensors: the strain range of the RDA inclination sensor is [-858.597,964.346] με, the strain range of the FBG strain sensor is [-983.022,116.582] με, and the strain range of the BG fiber optic sensor is [-79.230,46.406] με. The BG fiber optic sensor shows excellent zero drift performance in the three-hour drift resistance experiment. BG fiber optic sensor showed excellent anti-zero drift performance.

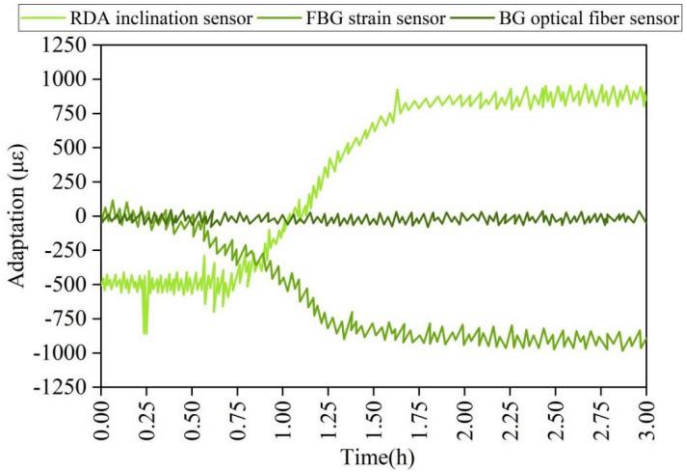

Figure 7: Anti-zero-drift performance of the three types of sensors

3.1.3 Comparison of proposed static performance against reciprocation

The performance of the sensors against reciprocating anthropomorphic forces was examined by concrete model tests. Three types of sensors were placed at the same locations in a large scale reinforced concrete pier model with small shear-to-span ratio and the reciprocating anthropomorphic force was applied to the model until the model was destroyed. Fig. 8 shows the displacements of the three types of models under the reciprocating anthropomorphic force. the BG fiber optic sensors showed small displacements only at the moment of applying the anthropomorphic force, and the rest of the moments remained at rest, with the overall

displacements in the range of -5.959~8.710 mm, while the RDA inclination sensors (-87.504~-87.504 mm) and the FBG strain sensors (-56.537~42.071 mm), and with the reciprocal application of the proposed static force, the sensors are displaced even when they are not stressed, making it difficult to continuously collect bridge health monitoring data at a given location.

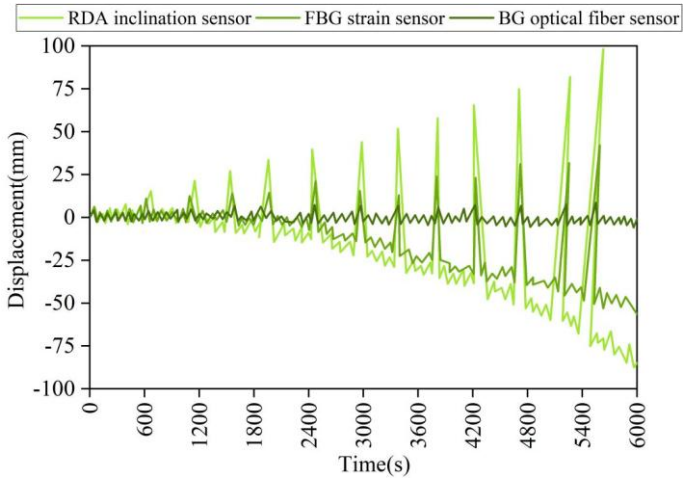

Figure 8: The displacement values of the three types of models

Comparing the basic performance of different sensors, the BG fiber optic sensor selected in this paper has stronger application advantages in three aspects: anti-electromagnetic interference, anti-drift, and anti-reciprocal proposed static force. This is related to both the material properties of the optical fiber and its acquisition method.

3.2 Analysis of the effect of identification of modal parameters of bridge structures

3.2.1 Signal Time-Course Curve and Power Spectrum Identification

The examined BG fiber optic sensors were applied to bridge A health monitoring data acquisition. After collecting and completing the demodulation of the optical signals, the analysis and identification of the structural modal parameters of Bridge A were processed using the HHT method. From the data, 1 segment record from one of the monitoring points in the middle section of the bridge was selected as the analyzed signal. The time profile of the signal of this segment is given in Fig. 9. The power spectrum of the segment signal obtained by FFT variation is given in Fig. 10. The time-range curve of 1800s of this segment signal shows regular 3 times fluctuation, and the vibration frequency is between 0 and 21 Hz, while the power spectrum also shows 3 times variation of the amplitude of this signal. Overall, the signal is consistent with the variation of the bridge structure when it is affected by external influences, and can be continued to EMD decomposition and IMF component curve calculation.

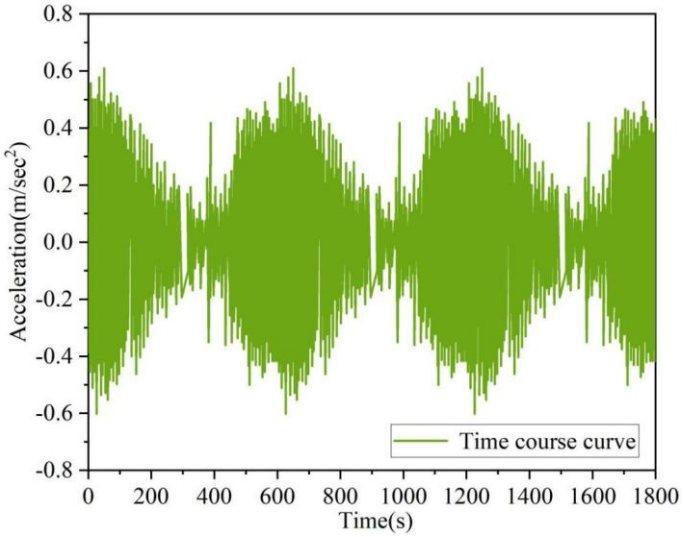

Figure 9: The time course curve of the signal

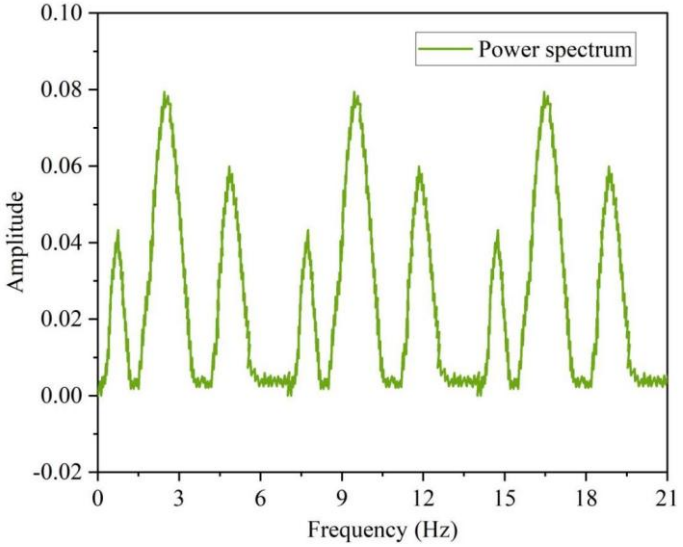

Figure 10: Power spectrum obtained by the FFT transformation of the signal

3.2.2 Free decay curves and their log-amplitude curve fitting

Applying the random reduction technique RDT to the IMF component curves conforming to the frequency range of interest of the structure yields the corresponding light-green free decay curves of Fig. 11, which are essentially IMF components with the random component of the response removed. It is then HT transformed to obtain the corresponding dark green logarithmic magnitude function. Afterwards, the log magnitude curve is linearly fitted to obtain its slope, which in turn calculates that the component curve represents a signal frequency of 0.574 Hz and a damping ratio of 0.253%.

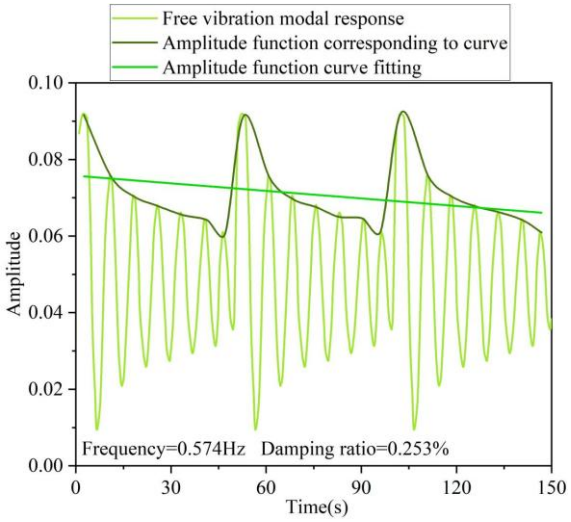

Figure 11: Free decay curve and its logarithmic amplitude curve and fitting

From the above analysis, it can be seen that the HHT method can be used to obtain stable and reliable results of modal parameter identification of bridge structures, which is a better method suitable for modal parameter identification of large bridge structures, comparing with the traditional processing method with simpler and faster steps.

3.3 Performance test of WPA-BP

3.3.1 Change in average fitness for iterative optimization of wolfpack algorithms

After completing the identification of the structural modal parameters of the bridge from the acquired signals, the modeled bridge A. The optimization effect of the wolf pack algorithm on the BP neural network is experimentally examined before real-time assessment of the bridge's health risk is implemented using the WPA-BP algorithm. Figure 12 shows the average adaptation of the wolf pack algorithm after 550 iterations. After 550 iterations, the average fitness decreases from 0.48614 to about 0.05221, which is a large decrease, and the algorithm iteration is more effective.

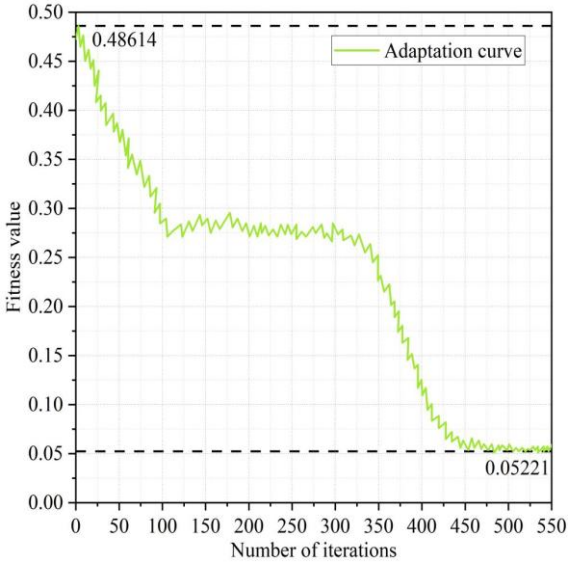

Figure 12: Average fitness value after 500 iterations of the wolf pack algorithm

3.3.2 Comparison of different algorithms to optimize the prediction effect of BP neural network

The optimal initial weights and thresholds etc. obtained from iterations are assigned to the BP neural network. In order to judge the optimization advantage of wolf pack algorithm on BP neural network, different algorithms (Particle Swarm Algorithm PSO, Genetic Algorithm GA) are selected to optimize the BP neural network, and at the same time, the optimized BP neural network is used to predict the health risk of bridges and compared with the actual values.

Figure 13 compares the risk prediction effect of 50 locations of bridges after optimizing the BP neural network with different algorithms.The actual risk occurrence probability of 50 bridge locations is 0.043~0.979, while the predicted risk occurrence probability of the WPA-BP is 0.091~0.989, the predicted risk occurrence probability of the PSO-BP is 0.008~0.802, and the GA-BP's Combined with the fluctuation of the risk occurrence probability curve, it can also be judged that the predicted risk occurrence probability of WPA-BP is the closest to the actual risk occurrence probability. In other words, iteratively solving the optimal initial weights and thresholds using the wolf pack algorithm can more effectively improve the real-time prediction accuracy of BP neural network on bridge health.

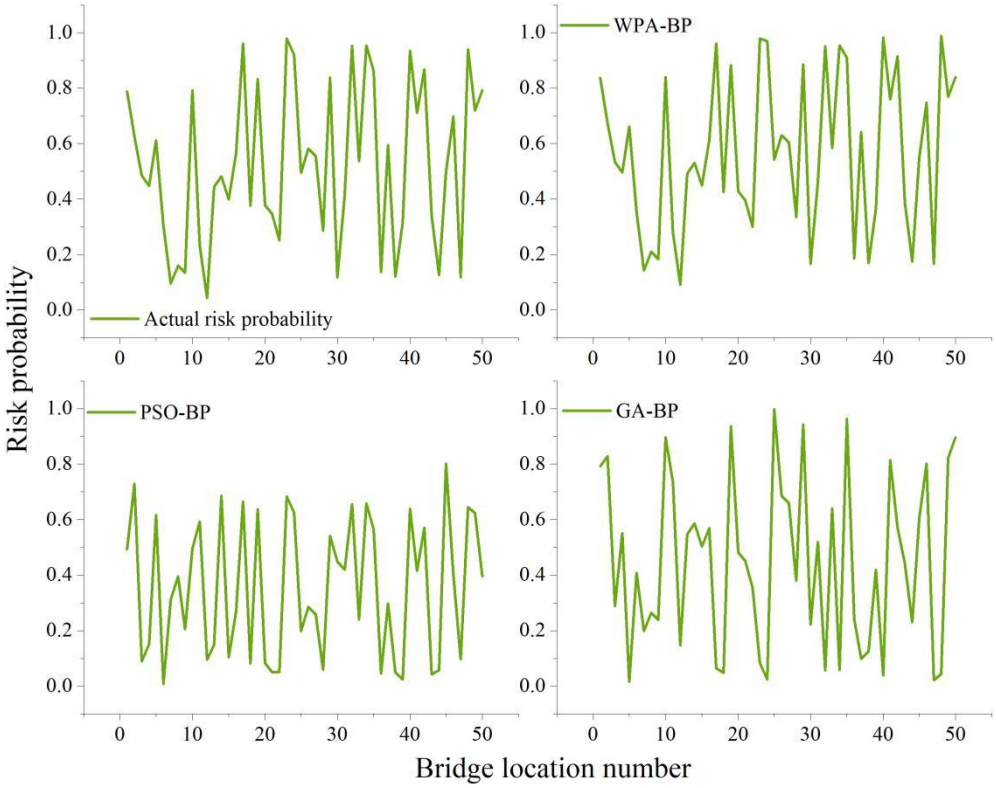

Figure 13: Risk prediction effects of BP neural networks optimized by algorithms

4 Conclusion

In this paper, a Bragg grating fiber optic sensor with good basic performance is used to collect bridge data, and the HHT method is used to identify the structural modal parameters of the bridge to construct a digital model that can reflect the health status of the bridge. The risk assessment of each part of the digital model is carried out by WPA-BP network to predict the bridge risk situation in that part, which provides decision support for timely repair and hazard reduction. The optimized WPA-BP network more quickly and accurately calculates the

probability of risk occurrence of 50 bridge parts as 0.091~0.989, respectively, which is closer to the actual risk probability of 0.043~0.979 than PSO-BP and GA-BP. The real-time risk assessment provides a guarantee for the durability of bridge health, which is also of greater benefit to the stability of urban transportation.

References

[1] Khatami, D., & Shafei, B. (2021). Impact of climate conditions on deteriorating reinforced concrete bridges in the US midwest region. Journal of Performance of Constructed Facilities, 35(1), 04020129.

[2] Wang, X., Wang, L., Wang, H., Ning, Y., Huang, K., & Wang, W. (2022). Performance evaluation of a long-span cable-stayed bridge using non-destructive field loading tests. Applied Sciences, 12(5), 2367.

[3] Ibrahim, A., Abdelkhalek, S., Zayed, T., Qureshi, A. H., & Mohammed Abdelkader, E. (2024). A comprehensive review of the key deterioration factors of concrete bridge decks. Buildings, 14(11), 3425.

[4] Konstandakopoulou, F. O. T. E. I. N. I. (2024). Health and Safety Challenges in Bridge Construction: A Comprehensive Review of Workplace Accidents. Engineering World, 6, 277-290.

[5] Han, Z. Y., Lei, J. Q., Li, G. X., & Wang, W. Q. (2025). Prevention and Safety Research of Bridge Life Cycle Risk Accidents. Int. J. Civ. Infrastruct, 8, 47-54.

[6] Gatti, M. (2019). Structural health monitoring of an operational bridge: A case study. Engineering Structures, 195, 200-209.

[7] Catbas, N., & Avci, O. (2023, June). A review of latest trends in bridge health monitoring. In Proceedings of the Institution of Civil Engineers-Bridge Engineering (Vol. 176, No. 2, pp. 76-91). Thomas Telford Ltd.

[8] Santarsiero, G., Masi, A., Picciano, V., & Digrisolo, A. (2021). The Italian guidelines on risk classification and management of bridges: Applications and remarks on large scale risk assessments. Infrastructures, 6(8), 111.

[9] Poli, F., Bado, M. F., Verzobio, A., & Zonta, D. (2025). Bridge structural safety assessment: a novel solution to uncertainty in the inspection practice. Structure and Infrastructure Engineering, 21(3), 421-435.

[10] Dorafshan, S., & Maguire, M. (2018). Bridge inspection: Human performance, unmanned aerial systems and automation. Journal of Civil Structural Health Monitoring, 8(3), 443-476.

[11] Rizzo, P., & Enshaeian, A. (2021). Challenges in bridge health monitoring: A review. Sensors, 21(13), 4336.

[12] Abdallah, A. M., Atadero, R. A., & Ozbek, M. E. (2022). A state-of-the-art review of bridge inspection planning: Current situation and future needs. Journal of Bridge

Engineering, 27(2), 03121001.

[13] Arshad, T., Karim, A., & Rarasati, A. D. (2024). Factors Influencing Bridge Inspection in Developing Countries, Challenges and Future Directions: A Systematic Literature Review. Smart City, 4(1), 7.

[14] Nie, Z., Lin, J., Li, J., Hao, H., & Ma, H. (2020). Bridge condition monitoring under moving loads using two sensor measurements. Structural Health Monitoring, 19(3), 917-937.

[15] Lu, R., & Judd, J. (2022). Field-deployable fiber optic sensor system for structural health monitoring of steel girder highway bridges. Infrastructures, 7(2), 16.

[16] Joksimović, N., & Brajović, L. (2023). Challenges and potential of fiber optic sensors for structural health monitoring of bridges: a review. In Proceedings of the 20th International Symposium of MASE, Skopje, North Macedonia, 28–29 September 2023. MASE-Macedonian Association of Structural Engineers Faculty of Civil Engineering, Blvd. Partizanski odredi No. 24 P. Box. 560, 1000 Skopje, Republic of North Macedonia.

[17] Taher, S. A., Li, J., Jeong, J. H., Laflamme, S., Jo, H., Bennett, C., ... & Downey, A. R. (2022). Structural health monitoring of fatigue cracks for steel bridges with wireless large-area strain sensors. Sensors, 22(14), 5076.

[18] Ajai Adarsan, K., Rajalakshmi, S., Suryanarayanan, T., Dharaneshwaran, S. P., & Nandhakumar, P. (2025). A Review on Application of Nanosensors for Monitoring the Structural Health of Bridges. Journal of Public Transportation, 4(1), 38-59.

[19] Nguyen, T. Q., Nguyen, T. A., & Nguyen, T. T. (2022). PSD characteristics for the random vibration signals used in bridge structural health monitoring in Vietnam based on a multi-sensor system. International Journal of Distributed Sensor Networks, 18(9), 15501329221125110.

[20] Xie, Y., Zhang, S., Meng, X., Nguyen, D. T., Ye, G., & Li, H. (2024). An innovative sensor integrated with GNSS and accelerometer for bridge health monitoring. Remote Sensing, 16(4), 607.

[21] Daijun, W. A. N. G., Tiantu, Z. H. O. U., Junmin, F. U., Xing, C. H. E. N., Shuai, L. U., & Zheng, Y. U. (2023). Research on multi-source and heterogeneous data integration of large bridge health monitoring system. Journal of China & Foreign Highway, 43(2), 100-106.

[22] Tong, X., Song, S., Wang, L., & Yang, H. (2018). A preliminary research on wireless cantilever beam vibration sensor in bridge health monitoring. Frontiers of Structural and Civil Engineering, 12(2), 207-214.

[23] Liyakat, K. K. S., Khadake, S. B., Galani, K., Patil, K. B., Dhavale, A., & Sarik, S. D. (2025, March). AI-Powered-IoT (AIIoT) based Bridge Health Monitoring using Sensor Data for Smart City Management-A KSK Approach. In 2025 7th International Conference on Intelligent Sustainable Systems (ICISS) (pp. 296-305). IEEE.

[24] Islam, M. M. (2025). Machine learning-based predictive modeling for assessing bridge

load capacity using real-time sensor data. Journal of Sustainable Development and Policy, 4(03), 01-37.

[25] Maroni, A., Tubaldi, E., McDonald, H., & Zonta, D. (2023). Monitoring-based adaptive water level thresholds for bridge scour risk management. Reliability Engineering & System Safety, 238, 109473.

[26] Qi, J. (2024). Bridge safety assessment and management strategies under long-term operating conditions. structure, 106.

[27] Chan, R. W., & Iwata, T. (2025). Risk Mitigation of a Heritage Bridge Using Noninvasive Sensors. Sensors, 25(12), 3727.

[28] Zhang, P., Wen, X., Fang, J., Li, Z., Pang, B., Lu, M., ... & Wang, F. (2025). Structural Collapse Risk Assessment of Steel Tube Coupler Scaffold Based on BP Neural Network and Sensor Optimization. Engineering Research Express.

[29] Hu, Y. (2025, September). Design of Bridge Collapse Risk Early Warning System Based on BeiDou Positioning and Implementation. In Proceedings of the 2025 2nd International Conference on Virtual Reality, Image and Signal Processing (pp. 178-183).

[30] Geng, Z., Zhang, C., Jiang, Y., Pugliese, D., & Cheng, M. (2025). Integrating multi-source data for life-cycle risk assessment of bridge networks: a system digital twin framework. Journal of Infrastructure Preservation and Resilience, 6(1), 9.